*Angewandte Chemie International Edition*

Angewandte International Edition Chemie

How to cite: *Angew. Chem. Int. Ed.* **2026**, e8043102
doi.org/10.1002/anie.8043102

RESEARCH ARTICLE

# Nature-Inspired Organic–Inorganic Hybridization Enables High-Temperature and Multicolor Organic Phosphorescence

Aoyuan Cheng[1,2] | Chengze Yang[1] | Hongping Liu[1] | Shikai Yu[3] | Xinrui Li[3] | Zheng Gong[1] | Baicheng Zhang[1] | Hailin Qiu[4] | Kan Hu[1] | Tao Wang[3] | Guoqing Zhang[1,2]

[1]Hefei National Research Center for Physical Sciences at the Microscale, University of Science and Technology of China, Hefei, China | [2]Hefei National Laboratory, University of Science and Technology of China, Hefei, China | [3]Beijing Key Laboratory of Construction Tailorable Advanced Functional Materials and Green Applications, School of Materials Science and Engineering, Beijing Institute of Technology, Beijing, China | [4]Orient KOJI Limited, Tianjin, China

**Correspondence:** Tao Wang (wt@bit.edu.cn) | Guoqing Zhang (gzhang@ustc.edu.cn)

**Received:** 16 March 2026 | **Revised:** 23 April 2026 | **Accepted:** 12 May 2026

**Keywords:** high-temperature afterglow | hydroxyapatite | organic–inorganic hybrids | room-temperature phosphorescence | tunable luminescence

## ABSTRACT

Organic room-temperature phosphorescence (RTP) has shown diverse practical applications; however, most organic RTP materials exhibit poor thermal resistance, with afterglow vanishing above ambient temperatures. Inspired by robust afterglow in natural minerals, we introduce a general organic–inorganic hybridization strategy that functionally replaces metallic dopants with organic chromophores. Specifically, carboxylated polycyclic aromatic hydrocarbons are molecularly embedded into the hydroxyapatite (**HAP**) lattice via an in situ co-precipitation method. The resulting artificial minerals exhibit strong and tunable RTP from organic chromophores with quantum yields of up to 31.1% and afterglow exceeding 10 s. By incorporating carboxylated triphenylamine, **TPA-3COOH**, into **HAP**, the obtained **TPA-3COOH/HAP** can even exhibit organic phosphorescence at 500 K. Mechanistic investigations reveal that the **HAP** lattice not only suppresses triplet nonradiative decay but also promotes the generation of triplet excitons via local electric-field-induced charge-transfer (CT) states and energy traps. This strategy is broadly applicable to various $\pi$-conjugated chromophores, enabling multicolor afterglows. Furthermore, solution-processable RTP-active artificial minerals and hydrogels are prepared to demonstrate the potential in UV-responsive sensing and medical treatment. This work provides a powerful platform for "lighting up" tunable organic RTP in artificial minerals.

## 1 | Introduction

The rapid development of optoelectronic devices and sensing technologies has driven the demand for versatile luminescent materials beyond those exhibiting only prompt fluorescence [1–6]. Organic room-temperature phosphorescence (RTP), emission from triplet excited states, generally exhibits long-lived and tunable luminescence, making it a promising candidate for versatile applications, like information storage [7–10] and afterglow display [11–14]. However, the intrinsic susceptibility of organic long-lived RTP renders it vulnerable to nonradiative deactivation pathways, including molecular vibrations, rotations, and collisions [15]. Consequently, long-lived RTP afterglow is only observed when molecular motions are effectively suppressed.

One widely adopted strategy involves embedding phosphors in viscous polymer matrices [16–19], where the translational degree of freedom is largely eliminated with vibrational and rotational freedoms mitigated. Despite the convenience of using polymers to sustain RTP, most polymer networks are permeable

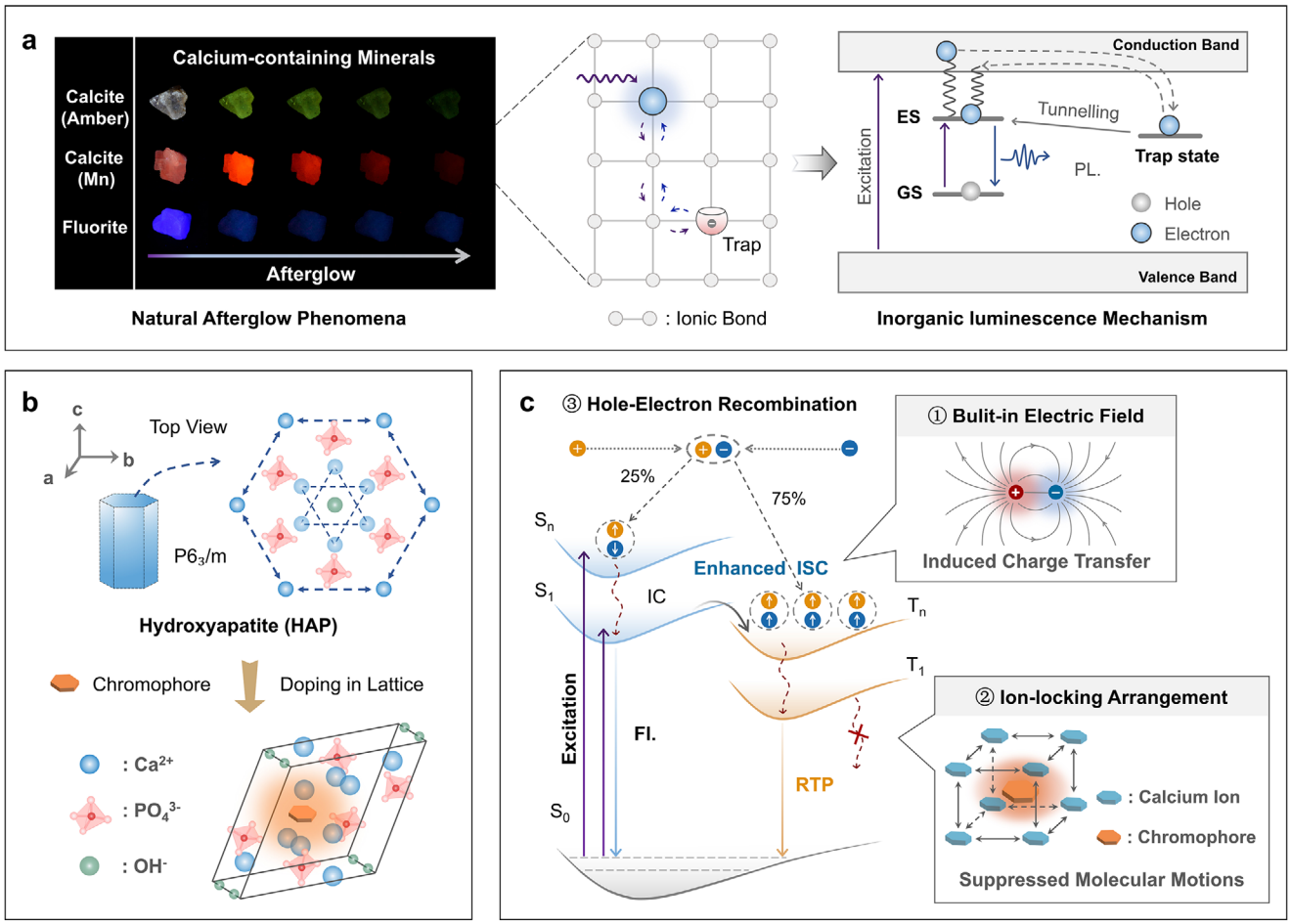


**FIGURE 1** | Design concept for triggering triplet-mediated RTP in inorganic minerals. (a) Photos showing RTP afterglows from representative calcium minerals and the schematic of the energy trap-assisted RTP mechanism of natural minerals. The trapped electrons can be released via thermal activation and the tunneling effect. (b) Schematic illustration of the **HAP** structure and its doping system. (c) Simplified Jablonski diagram depicting the triplet-mediated RTP mechanism in the organic–inorganic doping system with enhanced ISC and suppressed nonradiative transitions. GS: ground state; ES: excited state; Fl: fluorescence; IC: internal conversion.

to molecular oxygen (triplet quencher) except for a few examples, such as polyvinyl alcohol and polyamides [20, 21]. To address this limitation, alternative protective media such as crystals and glasses of all sorts have also been explored [22–25]. Despite better performance against oxygen penetration, these media are not without drawbacks. For example, Kasha and Lewis first demonstrated green afterglow from fluorescein using vitrified boric acid glass in the 1940s [26]; however, this material is hygroscopic and quickly decomposes under ambient conditions, leading to diminished RTP performance. Moreover, these organic RTP systems typically exhibit relatively poor thermal resistance, with triplet emission becoming silent above room temperature.

In contrast, inorganic minerals have rarely been explored as media for organic RTP, despite their well-documented natural afterglow phenomena [27, 28]. For example, several calcium-containing minerals including common calcite ($CaCO_3$) and fluorite ($CaF_2$) are known to exhibit afterglow of various colors after absorbing light (Figure 1a). The so-called phosphorescence emissions in calcium minerals occur when photoexcited electrons, trapped by lattice defects or metal dopants, are slowly released radiatively. Although synthetic calcite or fluorite exhibits effective RTP, they typically need high temperatures for preparation and lack post-processibility [29, 30], making precise control of luminescence characteristics challenging. Fortunately, these limitations can be addressed by hydroxyapatite ($Ca_5(PO_4)_3OH$, **HAP**), a calcium phosphate with a close-packed hexagonal structure (space group: P6$_3$/m) that can be prepared and processed under ambient conditions [31, 32], which exhibits excellent compatibility with organic matrices [33]. Inspired by mineral afterglow, we conceive that **HAP**'s phosphorescence can be activated by incorporating organic chromophores as trace components in the lattice (Figure 1b). In this design, organic chromophores are immobilized within the inorganic lattice via electrostatic interactions and function as modular triplet harvesters, enabling tunable emission behavior, while mild processing preserves chromophore integrity.

To verify this design, we develop a class of organic–inorganic hybrid phosphors by molecularly doping carboxylated polycyclic aromatic hydrocarbons (PAHs) into the **HAP** lattice. Comprehensive structural, photophysical, and theoretical investigations show that the introduction of PAHs generates local electric fields via interactions with calcium ions ($Ca^{2+}$), which can effectively

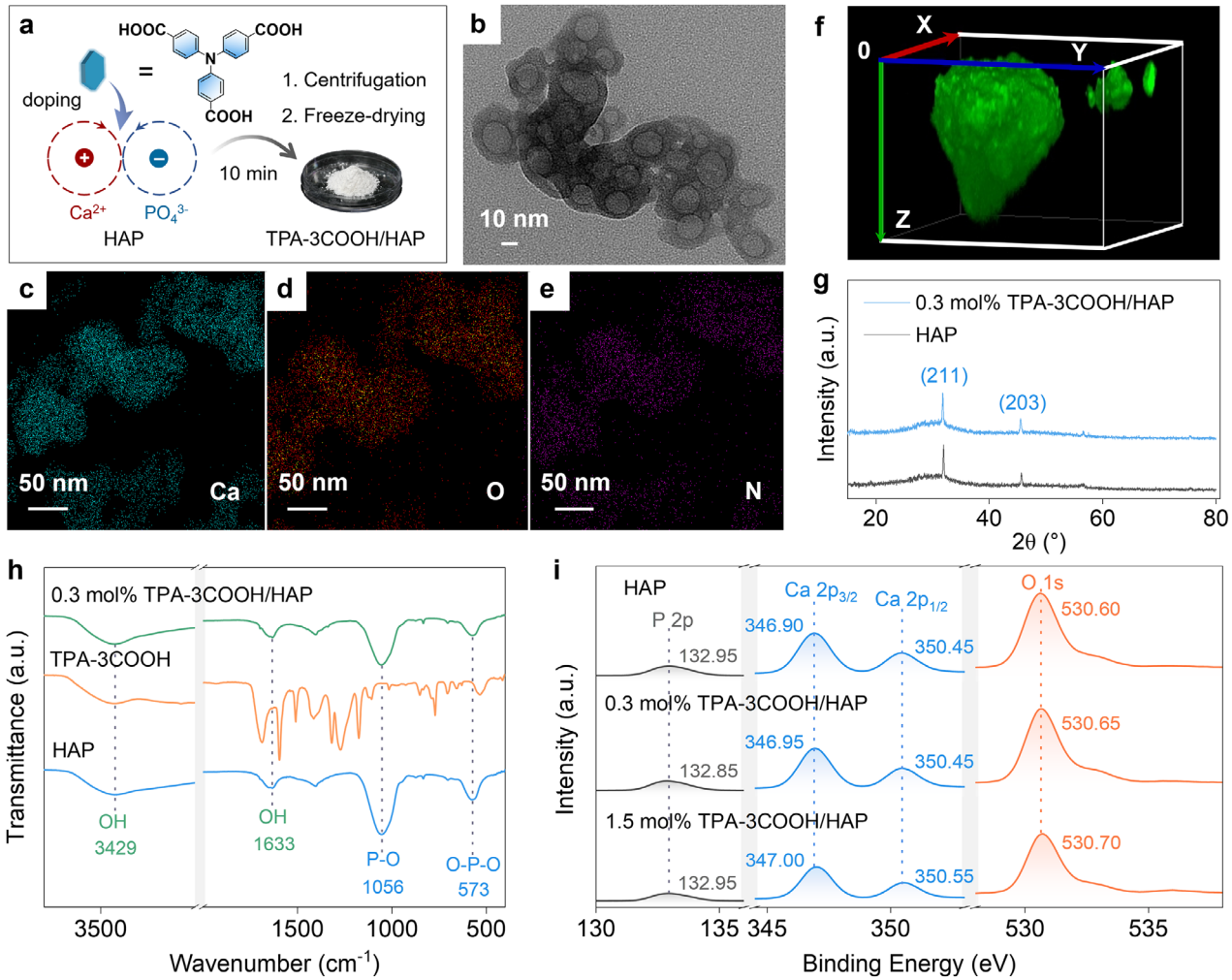


**FIGURE 2** | Structural characterization of organic chromophore-modified HAP. (a) Schematic illustration of the sample preparation process of **TPA-3COOH/HAP**. (b) TEM image of 0.3 mol% **TPA-3COOH/HAP**. (c–e) EDS mapping images of the Ca, O, and N elements of 0.3 mol% **TPA-3COOH/HAP**. (f) Confocal fluorescence imaging of 0.3 mol% **TPA-3COOH/HAP**. The image color does not represent the real emission color, which only reflects the PL signal. (g) Powder XRD patterns of **HAP** and 0.3 mol% **TPA-3COOH/HAP**. (h) Transmission FTIR spectra of **HAP**, **TPA-3COOH**, and 0.3 mol% **TPA-3COOH/HAP**. (i) High-resolution XPS spectra of **HAP** and **TPA-3COOH/HAP** with different chromophore loadings.

improve ISC of PAHs (Figure 1c). Simultaneously, $Ca^{2+}$ ions serve as molecular locks to restrict molecular motions of PAHs [34–37] and thus enhance organic RTP efficiency. Additionally, we also elucidate the positive role of inorganic energy traps in promoting the generation of organic triplet excitons. As a result, RTP quantum yields reach up to 31.1%, with visible phosphorescence persisting even at elevated temperatures exceeding 500 K. Unlike conventional calcite and fluorite, these PAH-doped **HAP** (PAH/**HAP**) materials achieve a highly tunable RTP afterglow, are prepared under ambient conditions within 10 min, and offer scalable potential for industrial production.

## 2 | Results and Discussion

### 2.1 | Synthesis and Structural Characterization

The PAH/**HAP** composites were prepared via a rapid in situ co-precipitation approach under ambient conditions within 10 min (Figures 2a and S1). To ensure that PAHs were in situ embedded into the lattice during the formation of **HAP**, an aqueous calcium chloride solution (150 mmol/L) was added dropwise into a hybrid solution of the carboxylated chromophore (alkalified with sodium hydroxide) and spectroscopically pure sodium phosphate (100 mmol/L) under continuous stirring. Because the organic chromophores are present in the initial precursor solution, the rapid crystallization of the calcium phosphate framework occurs concurrently with the strong electrostatic coordination between the calcium ions and the carboxylate groups. This simultaneous precipitation and ion-locking process traps the individual organic molecules within the growing inorganic lattice, preventing macroscopic organic aggregation and leading to a uniform organic–inorganic hybrid material. The resulting precipitates were collected by centrifugation and freeze-drying. The chromophore content is reported as a molar percentage relative to $Ca^{2+}$.

As a model system, the chromophore 4,4',4″-nitrilotribenzoic acid (**TPA-3COOH**) was selected to coordinate with $Ca^{2+}$, forming **TPA-3COOH/HAP** (Figure 2a). The solid-state $^{31}P$ nuclear magnetic resonance spectrum of 0.3 mol% **TPA-3COOH/HAP** displays a downfield shift compared with that of pure **HAP**

(Figure S2), indicating that the incorporation of the chromophore perturbs the **HAP** bulk ionic environment through electrostatic interactions and coordination between $Ca^{2+}$ and the chromophore. The $Ca^{2+}$ content was about 39.4 wt%, close to the theoretical value of 39.9 wt% (Table S1). Scanning electron microscopy (SEM) and transmission electron microscopy (TEM) were employed to examine the morphology and microstructure. The prepared 0.3 mol% **TPA-3COOH/HAP** exhibited uniform nanosphere sizes, with diameters of 20–30 nm (Figure S3). Like most reported **HAP** examples, **TPA-3COOH/HAP** displayed a hollow spherical structure (Figures 2b and S4), which could accommodate the chromophore via coordination during the in situ precipitation process. The energy-dispersive X-ray spectroscopy (EDS) mapping revealed that the doping system was successfully prepared, as evidenced by the evenly distributed nitrogen element of **TPA-3COOH** in **HAP** (Figures 2c–e and S5). The confocal fluorescence microscopy images demonstrated uniform luminescence throughout the sample, reflecting that the organic component was molecularly dispersed in **HAP** (Figures 2f and S6; Videos S1 and S2).

Notably, powder X-ray diffraction (XRD) confirmed the **HAP** structure, showing the characteristic peak at 31.7°, corresponding to the (211) plane (ICDD 01-074-9780), with a secondary peak assigned to the (203) plane at 46.6° (Figure 2g). The incorporation of the organic chromophore below 1.5 mol% does not disturb the **HAP** microstructure significantly, suggesting selective substitution at anionic sites by the chromophore without obviously altering the lattice integrity (Figure S7). This was further supported by Fourier transform infrared (FTIR) spectroscopy in the transmission mode, where the spectrum of **TPA-3COOH/HAP** closely resembled that of pristine **HAP** (Figures 2h and S8). This preservation of bulk crystallinity does not contradict the uniform molecular distribution; rather, it suggests that the chromophore is accommodated as localized defects or via selective substitution at anionic sites without causing global lattice collapse. We also conducted FTIR measurements in the attenuated total reflectance (ATR) mode (Figure S9), which is more sensitive to weak surface/near-surface absorptions. A clear characteristic peak at 1593 $cm^{-1}$, assigned to the aromatic C═C stretching vibration, becomes discernible for **TPA-3COOH/HAP** and becomes more pronounced when the chromophore content increases to 3.0 mol%. These results support the successful incorporation of the chromophore, while the absence of distinct chromophore signals in transmission FTIR is attributed to the sensitivity limit at low doping levels. In addition, in situ FTIR and Raman spectroscopy were performed to confirm the incorporation of the chromophore (Figure S10). The slight spectral differences between pure **HAP** and **TPA-3COOH/HAP** suggest that incorporating **TPA-3COOH** perturbs the P–O stretching vibrations in **HAP**.

Solid-state UV–vis absorption spectroscopy also confirmed successful doping, as the hybrid exhibited combined features of both **TPA-3COOH** and **HAP** in the 200–400 nm region (Figure S11). More importantly, we demonstrated the elemental compositions and presence of interactions between the chromophore and **HAP** using X-ray photoelectron spectroscopy (XPS). The elements Ca, P, C, O, and N were all identified in **TPA-3COOH/HAP** (Figures S12–S15; Tables S2–S4). The high-resolution XPS spectra of Ca 2p show two main peaks at 346.90 ($2p_{3/2}$) and 350.45 ($2p_{1/2}$) eV, which slightly shift to 347.00 and 350.55 eV, respectively, as the chromophore content increases to 1.5 mol% (Figure 2i). XPS spectra of P 2p and O 1s exhibit a similar phenomenon, indicating electronic perturbation caused by chromophore incorporation. Based on these systematic investigations, we can rationally conclude that the **TPA-3COOH/HAP** hybrid material was successfully prepared, with structural integrity of the **HAP** framework preserved and uniform dispersion of the organic chromophore achieved at the molecular level.

## 2.2 | Photophysical Investigations

To evaluate the RTP performance of **TPA-3COOH/HAP**, we conducted a series of systematic photophysical investigations. Note that all measurements were performed on as-prepared samples unless otherwise stated. First, the steady-state photoluminescence (PL) spectrum of 0.3 mol% **TPA-3COOH/HAP** shows a broad emission band with the PL maximum, $\lambda_{PL}$, at 430 nm (Figure 3a), and a fluorescence lifetime, $\tau_{Fl}$, of 3.0 ns (Figure S16). At room temperature, we observed a bright blue afterglow lasting for over 5 s (Figure 3a, inset). The phosphorescence spectrum detected by the time-gating technique reveals a relatively narrower emission band centered at 470 nm, with an associated phosphorescence lifetime, $\tau_{Ph}$, of 303.7 ms (Figure 3b). The total PL quantum yield (PLQY) is measured to be 36.5%, with prompt fluorescence and RTP contributions of 5.4% and 31.1%, respectively, as determined using a high-resolution time-correlated single photon counting (TCSPC) system integrated with a time-to-digital converter (TDC) (Figure 3b, inset), operating in a full-spectrum collection mode, rather than monitoring a specific wavelength.

To shed light on the origin of luminescence, we investigated the PL of **TPA-3COOH** in dilute 2-methyltetrahydrofuran (2-MeTHF, $1 \times 10^{-5}$ M). In solution, **TPA-3COOH** displays a blue-shifted steady-state PL spectrum with $\lambda_{PL}$ at 387 nm (Figure S17a), compared to 0.3 mol% **TPA-3COOH/HAP** in the solid state. At 77 K, **TPA-3COOH** in 2-MeTHF glass shows an obviously red-shifted steady-state PL with $\lambda_{PL}$ of 402 nm, alongside a shoulder peak at 462 nm (Figure S17b). We attribute these spectral shifts to conformational restrictions of the chromophore in different environments [38]. The time-gated PL measurement demonstrates that the emission at 462 nm originates from triplet states of **TPA-3COOH** (Figure S17c), indicating that the observed PL of 0.3 mol% **TPA-3COOH/HAP** arises from the organic chromophore. Note that the slight difference in the emission profiles between **TPA-3COOH** and **TPA-3COOH/HAP** is caused by restricted molecular motions that render specific vibronic levels as dark states, thereby narrowing the phosphorescence emission at lower temperatures. Further, we investigated PL behavior of **TPA-3COOH/HAP** at 298 K–77 K. As expected, phosphorescence evolves into a narrower emission as the temperature decreases (Figure S18). Time-resolve emission spectra (TRES) maps of **TPA-3COOH/HAP** recorded at 77 K exhibit similar emission band narrowing, compared to those at 298 K (Figure S19).

Notably, the measured 2D excitation–emission map of 0.3 mol% **TPA-3COOH/HAP** demonstrates excitation-independent RTP emission (Figure S20), which confirms a highly uniform local environment and the absence of diverse aggregate states, supporting the molecular-level dispersion of the chromophore within

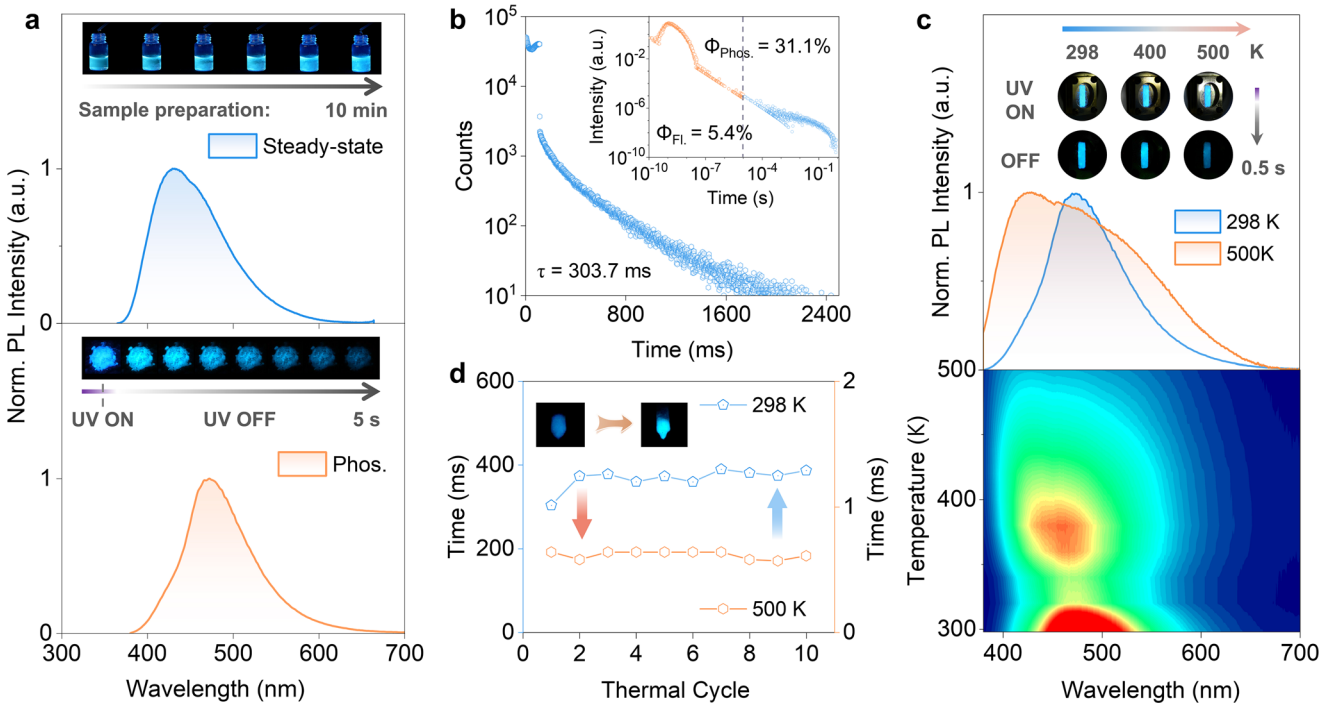


**FIGURE 3** | Photophysical investigations of 0.3 mol% TPA-3COOH/HAP recorded in air. (a) Steady-state (top) and delayed (gated time: 1–50 ms; bottom) PL spectra recorded at 298 K ($\lambda_{exc}$ = 365 nm). Insets: photos showing the formation of luminescent precipitates within 10 min (top) and RTP afterglow with UV off (bottom). (b) Phosphorescence decay profiles recorded at 470 nm at 298 K in air ($\lambda_{exc}$ = 372 nm). Inset: high-resolution PL decay profiles used to extract prompt fluorescence and RTP QYs based on the TDC–TCSPC technique. (c) Temperature-dependent delayed PL spectra with associated spectra recorded at 298 and 500 K ($\lambda_{exc}$ = 365 nm). Inset: photos showing phosphorescence afterglows at different temperatures. (d) RTP thermal resistance over 10 heating–cooling cycles. Inset: photos showing phosphorescence afterglow before heating and after 10-cycle thermal treatment.

the **HAP** matrix. It is worth noting that both steady-state and phosphorescence spectra remain almost unchanged even with an increase in chromophore loading up to 1.5 mol% (Figures S21 and S22). These results indicate that the **HAP** lattice effectively enables molecular-level dispersion of the organic chromophore.

Remarkably, the phosphorescence of the embedded chromophore remains observable at temperatures as high as 500 K (Figure 3c), despite a decrease in corresponding lifetimes (Figure S23). As the temperature increases from 298 to 330 K, the phosphorescence intensity at 470 nm gradually decreases due to enhanced nonradiative relaxation from molecular motions. Further temperature elevation to 370 K results in an increase in PL intensity and blue shift in the emission profile, due to the emergence of thermally activated delayed fluorescence (TADF) at ~430 nm (Figure S24). At 500 K, the TADF component even outcompetes the phosphorescence counterpart (Figure 3c). The associated PLQYs calculated based on TDC-TCSPC are shown in Figure S25. Notably, we found that the annealed 0.3 mol% **TPA-3COOH/HAP** sample exhibits longer phosphorescence lifetimes compared to the non-annealed counterpart (Figure S26). Thermogravimetry analysis (TGA) and differential scanning calorimetry (DSC) curves indicate that this intensity enhancement originates from the evaporation of residual water of crystallization, which induces tighter crystal packing and thereby suppresses triplet nonradiative deactivation (Figures S27 and S28). This structural ordering is supported by the powder XRD pattern of the sample after annealing at 500 K (Figure S29). Additionally, after subjecting the sample to 10 repeated heating-cooling cycles between 500 and 298 K, the RTP lifetime remains above 370 ms with no significant thermal fatigue (Figures 3d and S30–S32; Table S5), demonstrating superior thermal stability of the sample. The annealed sample displays brighter and longer RTP afterglow than its non-annealed counterpart (Figure 3d, inset). The unchanged emission behavior indicates the same emissive species (Figures S33 and S34). This confirms that the annealing process primarily induces tighter crystal packing and strengthens the coordination between the organic chromophore and the **HAP** lattice. In contrast, this excellent high-temperature PL performance is not present in polymers. For example, the phosphorescence of **TPA-3COOH** doped in polyvinyl alcohol (PVA) or polymethyl methacrylate (PMMA) is hardly detectable at 400 K (Figure S35), due to lack of rigid lattice confinement despite the presence of hydrogen bonds.

## 2.3 | Mechanistic Study

Although we have elucidated the role of the **HAP** lattice in suppressing the nonradiative exciton decay, it remains unclear how $Ca^{2+}$-chromophore interactions influence ISC. To clarify the underlying mechanism, we first conducted transient absorption measurements. The transient absorption spectra of 0.3 mol% **TPA-3COOH/HAP** display positive absorption bands peaking at 322, 352 and 401 nm (Figures 4a and S36), resulting from $S_1 \rightarrow S_n$ transitions, which decays with tens of picoseconds. Concurrently, two negative absorptions emerge at 339 and 385 nm, which correspond to ground-state bleaching (GSB) since **TPA-3COOH/HAP**

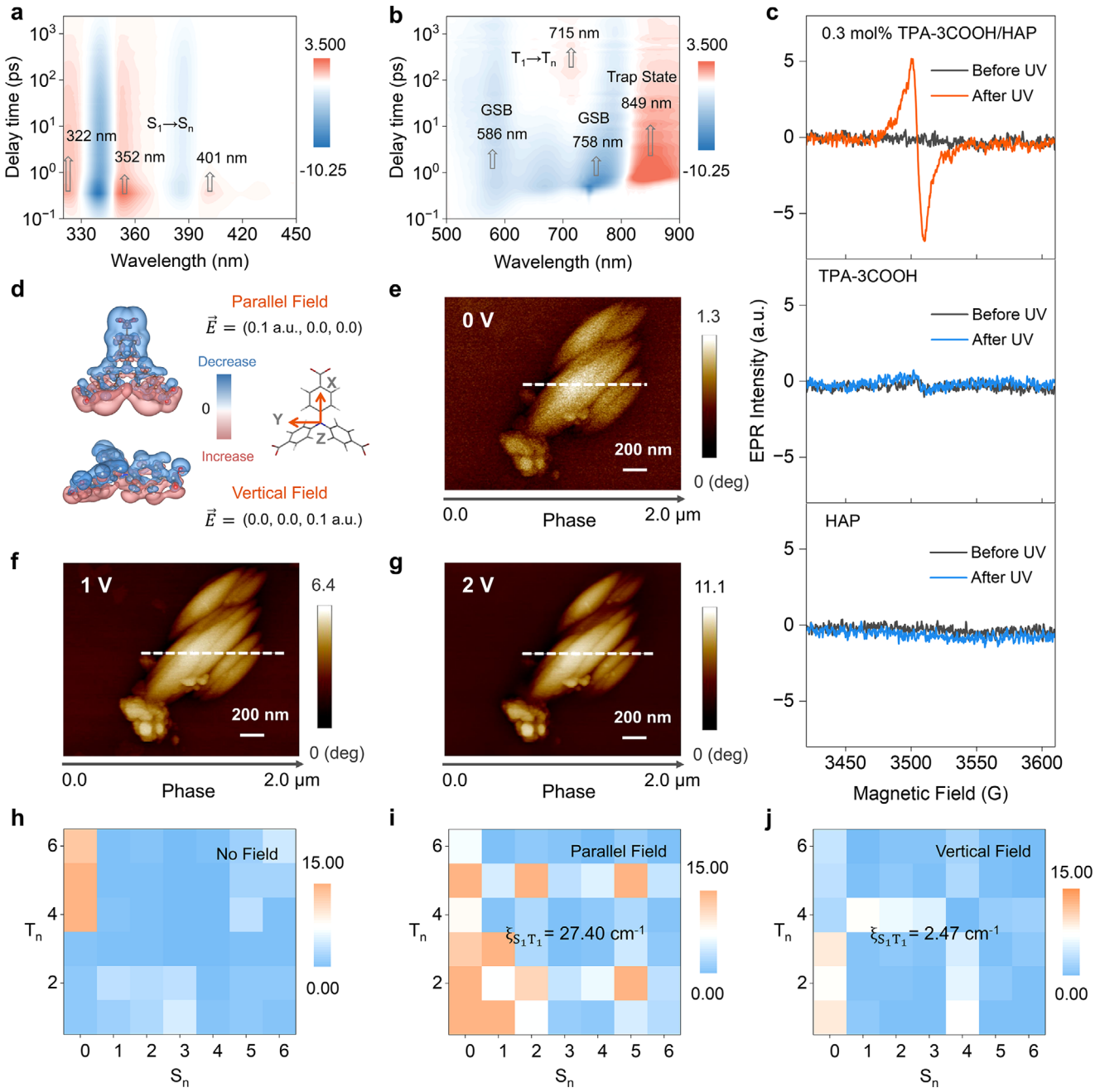


**FIGURE 4** | Mechanistic elucidation of the enhanced RTP. (a–b) Transient absorption spectra of 0.3 mol% **TPA-3COOH/HAP** in the range of (a) 320–450 nm and (b) 500–900 nm as a function of delay time ($\lambda_{exc}$ = 365 nm; pump power: 1 μJ/cm$^2$ per pulse). (c) EPR spectra of **HAP**, **TPA-3COOH** and 0.3 mol% **TPA-3COOH/HAP** in the solid state before and after 365 nm UV light treatment for 90 s, respectively. (d) Calculated change in electron density distribution upon applying parallel and vertical electric fields (isovalue: 0.003). Blue and red denote the decrease and increase in electron density, respectively. (e-g) EFM phase images of 0.3 mol% **TPA-3COOH/HAP** powder acquired under the applied biases of (e) 0 V, (f) 1 V, and (g) 2 V. White dotted lines indicate phase shift as a function of the lateral position for comparison (see Figure S44). (h-j) Calculated SOC constants between singlet and triplet excited states (h) without the electric field, (i) with the applied parallel electric field, and (j) with applied vertical electric field.

exhibits associated absorptions in this range (Figure S11). Differing from the positive absorptions, these GSB signals persist exceeding 2 ns. This can be attributed to shallow energy traps in **HAP** [39–41], thus prolonging exciton lifetimes. To verify this, we extended the transient absorption measurements to 500–900 nm for both **TPA-3COOH/HAP** and **HAP** (Figures 4b and S37). The spectra of **HAP** show varying negative absorption bands between 500 and 640 nm, arising from GSB caused by varied defect-induced traps, such as oxygen vacancies, hydroxyl migration, and $Ca^{2+}$ deficiencies [42–46]. Upon the incorporation of the chromophore, the GSB signals shift to longer wavelengths, with a notable redshift from 567 nm to 586 nm, indicating that chromophore–**HAP** interactions reshape the local traps (Figures 4b, S37 and S38). Similarly, the GSB features of **HAP** around 730 nm shift to 755 nm. The positive bands peaking at 849 nm are due to excited-state absorption from trap states

(trapped charges). Importantly, the spectra also exhibit a growing positive absorption at 715 nm within 0.1 ns, which persists for more than 2 ns (Figures S37 and S38). The fitted ISC rate is up to $8.76 \times 10^{10}$ $s^{-1}$ (Figure S39), suggesting a rapid singlet–triplet ISC of the organic chromophore. This indicates that trap states likely slow singlet exciton deactivation, thereby increasing the possibility of ISC. Using the Hoogenstraaten method, the estimated trap depth is 0.125 ± 0.02 eV based on the thermoluminescence (TL) spectra (Figure S40).

We next conducted electron paramagnetic resonance (EPR) measurements to demonstrate the role of energy traps in capturing excitons. Without photoexcitation, no radical signal was detected in **HAP**, **TPA-3COOH**, and 0.3 mol% **TPA-3COOH/HAP**. However, following 365 nm UV irradiation for 90 s, **TPA-3COOH/HAP** showed an intense radical signal after cessation of excitation (Figure 4c), which remained detectable even after 10 min (Figure S41). Note that the absence of the hyperfine spectral structure is likely due to strong spin–spin interactions and shortened transverse relaxation. The corresponding *g* value is 2.0114, which is higher than that of conventional **TPA**-based radical cations ($g = 2.002$–$2.005$) [47]. This positive shift suggests that the unpaired spin is substantially delocalized onto atoms with larger spin–orbit coupling (SOC), most plausibly the oxygen atoms of the carboxyl groups and, potentially, surface oxygen sites of the **HAP** matrix. This is consistent with the strong coordination interaction between **TPA-3COOH** and **HAP**. In contrast, **HAP** and **TPA-3COOH** showed negligible EPR signal under identical irradiation conditions. These results demonstrate that the radical signal recorded in **TPA-3COOH/HAP** arises from photogenerated radical species (or charge-separated excitons) trapped in **HAP** defects. Theoretically, the resulting separated holes and electrons can subsequently recombine to generate up to 75% triplet excitons, thereby enabling efficient RTP. Temperature-dependent bi-exponential fitting of the delayed PL lifetimes indicates that the observed delayed emission reflects the combined contributions of triplet emission and trap-assisted charge release and recombination (Figure S42).

Considering that the electrostatic interactions between $Ca^{2+}$ and the organic chromophore can theoretically generate a built-in electric field, we assume that the formed local electric field may alter the electron density distribution of the chromophore. To verify this assumption, we conducted theoretical modelling based on the density functional theory (DFT) at the PBE0/def2-SVP level [48, 49]. Based on the hexagonal packing model of **HAP**, the distances between $Ca^{2+}$ ions and the center of **HAP**'s hexagonal lattice packing are ca. 3.4 (inner layer) and 4.0 Å (outer layer) (Figure S43). Assuming the chromophore is positioned midway between $Ca^{2+}$ and the hexagonal packing center, the strength of the established electric field is estimated to range from $7.20 \times 10^{10}$ to $9.96 \times 10^{10}$ V/m. For simplification, a representative field strength of 0.1 a.u. was applied in the DFT modelling. As expected, the introduction of the electric field leads to the inhomogeneous electron density distribution (Figure 4d), like that of donor–acceptor molecules [50–53]. This reasonably explains why **TPA-3COOH/HAP** exhibits a broad structureless steady-state emission spectrum under photoexcitation (Figure 3a), owing to the charge-transfer (CT) contribution and conformational heterogeneity. It has been widely demonstrated that the formation of CT states can promote singlet–triplet ISC to generate triplet excitons for RTP [54–57]. Notably, the existence of the local electric field in **TPA-3COOH/HAP** can be experimentally validated by electrostatic force microscopy (EFM), as evidenced by the bias-dependent phase-shift contrast (Figures 4e–g). Upon the removal of the applied bias, the phase shift along the white dotted line can return to its initial state, indicating the excellent reversibility (Figure S44).

Further, we investigated how the electric field influences the singlet–triplet SOC. Without the electric field applied, the calculated SOC constants indicate that efficient ISC only occurs between $S_1$ and high-lying triplet excited states (Figure 4h). However, upon introducing a parallel electric field, significantly enhanced ISC between $S_1$ and both low-lying and high-lying triplet excited states can be observed (Figure 4i). As the electron density redistribution spans the entire molecular backbone uniformly with the vertical electric field applied, the ineffective generation of CT states fails to effectively promote ISC (Figure 4j). This electric-field-enhanced ISC was also experimentally demonstrated using a lab-made setup (Figure S45). The measured prompt fluorescence lifetime under a 20 V DC bias is 2.9 ns, which is nearly identical to the lifetime without the bias ($\tau_{Fl} = 3.0$ ns) (Figure S46). This outcome is because the applied electric field modulates both the intrinsic singlet radiative transition and the ISC rate by altering the excitonic transition dipole moment. These concurrent modulations result in an overall lifetime that remains largely unchanged, while still facilitating enhanced triplet generation. However, upon applying the bias, the steady-state PL intensity gradually decreased, whereas the delayed PL (RTP) intensity increased (Figure S47), indicating enhanced ISC that depletes singlet excitons while increasing triplet excitons. This provides direct spectroscopic evidence that the electric field manipulates the excited state mixing and promotes ISC. Notably, because the prepared **TPA-3COOH/HAP** is an insulating dielectric and the system lacks charge-injection and transport layers (Figure S48), the conventional electroluminescence mechanism via charge recombination is not favored in this case. We also demonstrated that RTP could be activated in other Ca-based inorganics, like $CaF_2$ and $CaCO_3$, which exhibited similar emission profiles (Figure S49). This finding further validates the positive role of the local electric field in activating RTP.

Consequently, these findings reveal three key roles of **HAP** in enhancing the organic RTP emission of the embedded organic chromophore (see Figure 1c): improving ISC through electric-field-induced CT state formation, capturing photoexcited electrons, enabling subsequent hole–electron recombination for generation of abundant triplet excitons, and suppressing nonradiative deactivation of triplet excitons through spatial confinement.

## 2.4 | Generality of the Design Strategy

To demonstrate the generality of this organic–inorganic doping strategy in triggering efficient RTP, we extended our molecular scope to include a series of $\pi$-conjugated organic chromophores. Although both the $S_1$ and $T_1$ states in these systems are dominated by the $\pi \rightarrow \pi^*$ character, bright RTP was recorded. First, carboxylated 1,3,5-triphenylbenzene (**1,3,5-Tpp**) was used instead of **TPA-3COOH**. At a chromophore loading of 0.3 mol%, **1,3,5-**

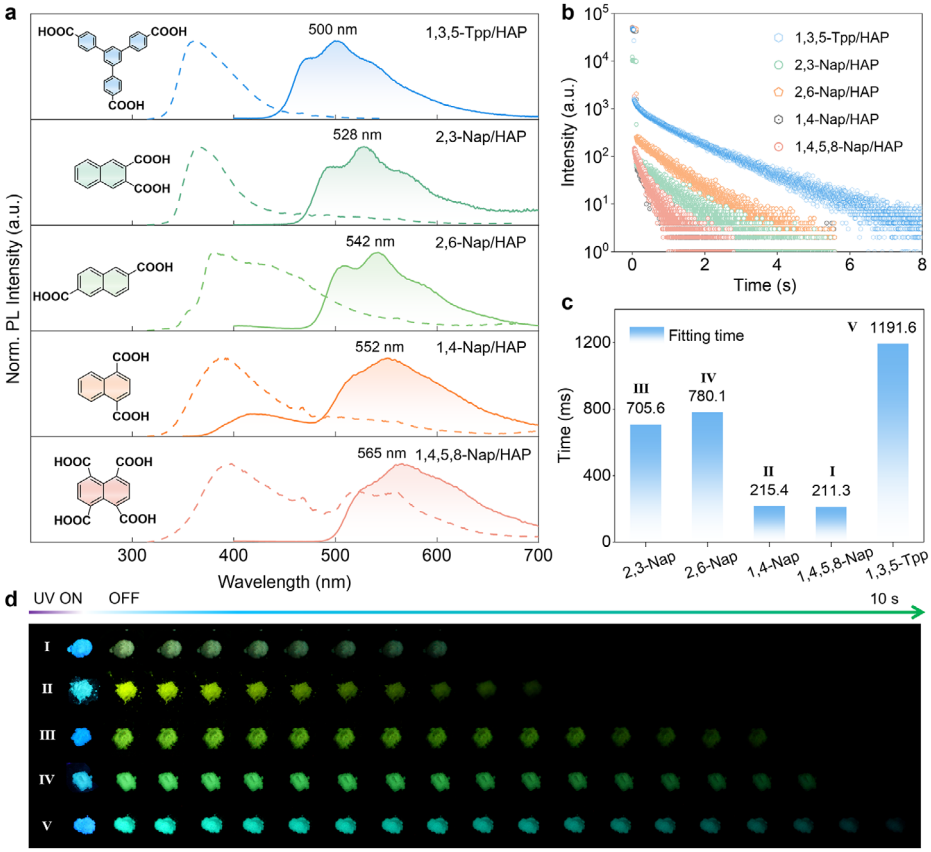


**FIGURE 5** | Photophysical investigations of 0.3 mol% $\pi$-conjugated chromophores in HAP recorded at 298 K in air. (a) Steady-state (dashed line; $\lambda_{exc}$ = 300 nm) and delayed (solid line; gated time: 1–50 ms; $\lambda_{exc}$ = 254 nm) PL spectra recorded at 298 K in air. (b-c) Phosphorescence decay profiles and fitting values ($\lambda_{exc}$ = 281 nm). (d) Photos showing RTP afterglows.

**Tpp/HAP** exhibits a steady-state PL spectrum with $\lambda_{PL}$ at 362 nm (Figure 5a). With a setup of 1 ms delay, the measured delayed PL spectrum reveals a structured RTP emission centered at 500 nm, characteristic of a typical $\pi \rightarrow \pi^*$ transition. To further explore structural diversity, we used carboxylated naphthalene derivatives instead of **1,3,5-Tpp** to prepare **2,6-Nap/HAP**, **2,3-Nap/HAP**, **1,4,5,8-Nap/HAP**, **1,4-Nap/HAP**. All samples exhibit structural characteristics similar to **TPA-3COOH/HAP** (Figures S50–S54), displaying broad steady-state PL spectra, and $^3(\pi \rightarrow \pi^*)$-like RTP emissions (Figure 5a). Interestingly, despite their structural similarity, these naphthalene-based chromophores show distinct PL features with varied RTP emission maxima, from 528 nm to 565 nm, with associated different excitation spectra (Figure S55). Reminiscent of the mechanism we have elucidated above, this divergence is attributed to differences in local built-in electric fields within **HAP**, which perturb the chromophores' excited-state electronic configurations.

Notably, besides major RTP bands in the 480–700 nm range, **1,4-Nap/HAP** has minor RTP emissions between 360–480 nm, attributed to emission from higher-lying triplet excited states ($T_2$). At 77 K, the $T_2$ emissions become more prominent in these organic chromophores due to suppressed $T_2$-$T_1$ vibronic coupling (Figures S56–S60). This multiple phosphorescence phenomenon has been thoroughly investigated in our previous work [58–61]. All these doping samples exhibit ultralong RTP lifetimes of up to 1191.6 ms (Figure 5b), alongside an afterglow exceeding 10 s (Figure 5c).

## 2.5 | Potential Applications

To demonstrate the tunable luminescence of this organic–inorganic doping system, we fabricated an "artificial mineral" by co-doping 0.15 mol% **TPA-3COOH** and 0.15 mol% **1,4,5,8-Nap** in **HAP** (**TPA-3COOH/1,4,5,8-Nap/HAP**). The 2D excitation–emission map, measured using time-gating technique, reveals excitation-dependent RTP emission, with two optimal excitation wavelengths at 294 and 360 nm corresponding to blue and yellow phosphorescence, respectively (Figure 6a). The Commission Internationale de l'Eclairage (CIE) coordinates shows that the RTP afterglow transitions from blue to yellow as the excitation wavelength changes from 254 and 365 nm, passing through the white emission region (Figure 6b). This observation suggests that the color of RTP afterglow can be used to visualize invisible UV light, as demonstrated by the UV-wavelength-dependent afterglow behavior (Figure 6c). Moreover, by incorporating terminal fluorophores as energy acceptors, multicolor afterglow samples were prepared via triplet-to-singlet energy transfer (Figure 6d; see Figure S61 for the associated sensitization spectra).

Additionally, performing in situ mineralization of 0.3 mol% **TPA-3COOH/HAP** within a polyacrylamide (PAM) aqueous solution (10.0% in $H_2O$, w/v), followed by chemical crosslinking using glutaraldehyde (2.0%, v/v), we obtained luminescent, mineralized PAM hydrogel materials exhibiting plasticity (Figure 6e). Given that **HAP** is widely recognized for its osteoconductive properties, these solution-processable, RTP-active **HAP**-based

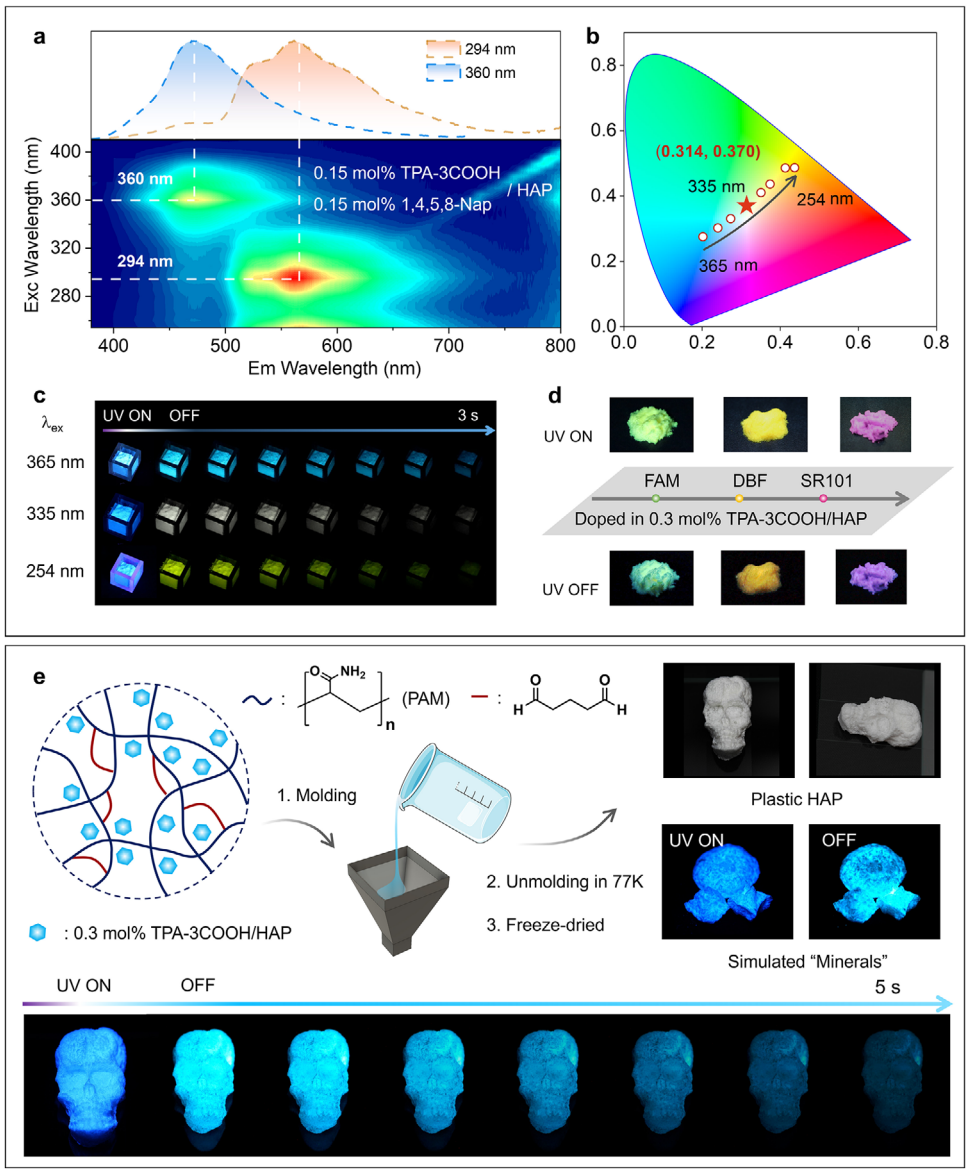


**FIGURE 6** | Demonstrations of potential applications. (a) 2D excitation–emission map of the artificial mineral **HAP** containing 0.15 mol% **TPA-3COOH** and 0.15 mol% **1,4,5,8-Nap**, recorded at 298 K in air using the time-gating technique (gated time: 1–50 ms). (b) CIE coordinates of RTP afterglows of **TPA-3COOH/1,4,5,8-Nap/HAP** with organic chromophores each doped at 0.15 mol%, showing color evolution under different excitation wavelengths. (c) Photos showing excitation-wavelength-dependent RTP afterglows of **TPA-3COOH/1,4,5,8-Nap/HAP**. (d) Multicolor afterglow samples generated by introducing fluorophores as energy acceptors, 5 wt% 5-carboxyfluorescein (**FAM**), dibromofluorescein (**DBF**) and sulforhodamine 101 (**SR101**). (e) Schematic illustration of the preparation of PAM hydrogels incorporating 0.3 mol% **TPA-3COOH/HAP** and the fabrication of corresponding RTP handcrafts.

hydrogels have promising potential for in situ monitoring of bone repair and regeneration.

## 3 | Conclusion

In summary, we have developed a versatile organic–inorganic doping strategy for enabling efficient and stable organic phosphorescence by integrating carboxylated PAHs into the **HAP** lattice. The preparation can be finished within 10 min, indicating an industrial potential for large-scale production. The resulting materials exhibit high RTP QYs of up to 31.1%, ultralong lifetimes, and excellent thermal robustness, with observable phosphorescence persisting beyond 500 K. Mechanistic investigations confirm that **HAP** enhances RTP via three synergistic effects: (1) promoting ISC through local electric-field-induced CT states, (2) trapping photoexcited charges to generate abundant triplet excitons, and (3) suppressing nonradiative decay through rigid spatial confinement. This strategy is generalizable across diverse $\pi$-conjugated chromophores, enabling multicolor RTP emissions including $T_2$-state-derived dual phosphorescence. We have also demonstrated the potential applications through the construction of RTP-active artificial minerals and hydrogels for sensing and medical treatment. Overall, these findings offer a

facile, scalable, and tunable approach toward high-performance organic RTP materials, bridging mineral-like rigidity and molecular design flexibility.

### Author Contributions

**Aoyuan Cheng:** investigation, writing – original draft, visualization, validation, methodology, data curation, conceptualization, writing – review and editing, software. **Chengze Yang:** investigation. **Hongping Liu:** methodology. **Shikai Yu:** investigation. **Xinrui Li:** investigation. **Zheng Gong:** methodology, investigation. **Baicheng Zhang:** methodology. **Hailin Qiu:** methodology. **Kan Hu:** methodology. **Tao Wang:** conceptualization, methodology, writing – review and editing, writing – original draft, funding acquisition, supervision, project administration, data curation, resources, software. **Guoqing Zhang:** writing – original draft, writing – review and editing, funding acquisition, methodology, conceptualization, formal analysis, supervision, resources.


### Acknowledgements

This work was financially supported by the National Natural Science Foundation of China (22505012, 22475204, and 225B2307), Beijing Natural Science Foundation (2252054), the Strategic Priority Research Program of the Chinese Academy of Sciences (XDB1300000), the Innovation Program for Quantum Science and Technology (2021ZD0303301), the USTC Bihe Youth Program for Interdisciplinary Innovation (BH-202507), and the Fundamental Research Funds for the Central Universities (WK9990000099). We also gratefully acknowledge financial support from the National Center for International Research on Intelligent Nano-Materials and Detection Technology in Environmental Protection (SDGH2402). This work received the support from the robotic AI-Scientist platform of the Chinese Academy of Sciences.


### Conflicts of Interest

The authors declare no conflicts of interest.

### Data Availability Statement

The data that support the findings of this study are available from the corresponding author upon reasonable request.

### References


1. C. Li, Z. Lou, M. Wu, et al., "Achieving Efficient Organic Room-Temperature Phosphorescence Through Acceptor Dendronization," *Journal of the American Chemical Society* 147 (2025): 18317–18326.

2. J. Zeng, S. Song, Y. Fu, X. Peng, B. Z. Tang, and Z. Zhao, "Purely Organic Room-temperature Phosphorescence Sensitizers for Highly Efficient Hyperfluorescence OLEDs," *Science Advances* 11 (2025): eadt7899..

3. G. Zhang, G. M. Palmer, M. W. Dewhirst, and C. L. Fraser, "A Dual-emissive-materials Design Concept Enables Tumour Hypoxia Imaging," *Nature Materials* 8 (2009): 747–751..

4. J. You, C. Yin, S. Wang, et al., "Responsive Circularly Polarized Ultralong Room Temperature Phosphorescence Materials With Easy-to-Scale and Chiral-Sensing Performance," *Nature Communications* 15 (2024): 7149.

5. W. Qiu, D. Liu, Z. Chen, et al., "Afterglow OLEDs Incorporating Bright Closely Stacked Molecular Dimers With Ultra-Long Thermally Activated Delayed Fluorescence," *Matter* 6 (2023): 1231–1248.

6. E. Hamzehpoor, C. Ruchlin, Y. Tao, C.-H. Liu, H. M. Titi, and D. F. Perepichka, "Efficient Room-temperature Phosphorescence of Covalent Organic Frameworks Through Covalent Halogen Doping," *Nature Chemistry* 15 (2023): 83–90..

7. L. Gao, J. Huang, L. Qu, et al., "Stepwise Taming of Triplet Excitons via Multiple Confinements in Intrinsic Polymers for Long-lived Room-temperature Phosphorescence," *Nature Communications* 14 (2023): 7252.

8. J. Guo, C. Yang, and Y. Zhao, "Long-Lived Organic Room-Temperature Phosphorescence From Amorphous Polymer Systems," *Accounts of Chemical Research* 55 (2022): 1160–1170.

9. L. Tu, Y. Chen, X. Song, W. Jiang, Y. Xie, and Z. Li, "Förster Resonance Energy Transfer: Stimulus-Responsive Purely Organic Room Temperature Phosphorescence Through Dynamic B–N Bond," *Angewandte Chemie International Edition* 63 (2024): e202402865.

10. Y. Li, L. Li, R. Shao, et al., "High-Temperature Phosphorescence of Carbon Dots by a Synergistic Locking Strategy," *ACS Applied Materials & Interfaces* 17 (2025): 23104–23113.

11. C. Si, T. Wang, A. K. Gupta, et al., "Room-Temperature Multiple Phosphorescence From Functionalized Corannulenes: Temperature Sensing and Afterglow Organic Light-Emitting Diode**," *Angewandte Chemie International Edition* 62 (2023): e202309718.

12. D. Cui, L. Zhang, J. Zhang, et al., "Hybrid Local and Charge-Transfer Material With Ultralong Room Temperature Phosphorescence for Efficient Organic Afterglow Light-Emitting Diodes," *Angewandte Chemie International Edition* 63 (2024): e202411588.

13. T. Wang, *Encyclopedia of Aggregation-Induced Emission*, ed. B. Z. Tang, Z. Zhao, and Z. Qiu, (Springer Nature Singapore, 2025), 1.

14. M. Singh, K. Shen, W. Ye, et al., "Achieving High-Temperature Phosphorescence by Organic Cocrystal Engineering," *Angewandte Chemie International Edition* 63 (2024): e202319694.

15. Q. Peng, H. Ma, and Z. Shuai, "Theory of Long-Lived Room-Temperature Phosphorescence in Organic Aggregates," *Accounts of Chemical Research* 54 (2021): 940–949..

16. D. Li, Z. Liu, M. Fang, J. Yang, B. Z. Tang, and Z. Li, "Ultralong Room-Temperature Phosphorescence With Second-Level Lifetime in Water Based on Cyclodextrin Supramolecular Assembly," *ACS Nano* 17 (2023): 12895–12902.

17. Y. Miao, F. Lin, D. Guo, et al., "Stable and Ultralong Room-temperature Phosphorescent Copolymers With Excellent Adhesion, Resistance, and Toughness," *Science Advances* 10 (2024): eadk3354.

18. H. Ju, H. Zhang, L. X. Hou, et al., "Polymerization-Induced Crystallization of Dopant Molecules: An Efficient Strategy for Room-Temperature Phosphorescence of Hydrogels," *Journal of the American Chemical Society* 145 (2023): 3763–3773.

19. M. Wu, Y. Guan, P. Wang, et al., "High-Temperature-Available Organic Blue Phosphorescence for Optical Waveguide," *Advanced Functional Materials* 35 (2025): 2505113.

20. D.-X. Ma, Z.-Q. Li, K. Tang, Z.-L. Gong, J.-Y. Shao, and Y.-W. Zhong, "Nylons With Highly-Bright and Ultralong Organic Room-Temperature Phosphorescence," *Nature Communications* 15 (2024): 4402..

21. H. Yang, Y. Wang, X. Yao, et al., "Efficient and Ultralong Room Temperature Phosphorescence From Isolated Molecules Under Visible Light Excitation," *Journal of the American Chemical Society* 147 (2025): 1474–1481.

22. S. Garain, S. N. Ansari, A. A. Kongasseri, B. Chandra Garain, S. K. Pati, and S. J. George, "Room Temperature Charge-Transfer Phosphorescence From Organic Donor–acceptor Co-Crystals," *Chemical Science* 13 (2022): 10011–10019..

23. W. Li, Q. Huang, Z. Mao, et al., "A Dish-Like Molecular Architecture for Dynamic Ultralong Room-temperature Phosphorescence Through Reversible Guest Accommodation," *Nature Communications* 13 (2022): 7423.

24. F. Nie and D. Yan, "Bio-sourced Flexible Supramolecular Glasses for Dynamic and Full-color Phosphorescence," *Nature Communications* 15 (2024): 9491..

25. O. Bolton, K. Lee, H.-J. Kim, K. Y. Lin, and J. Kim, "Activating Efficient Phosphorescence From Purely Organic Materials by Crystal Design," *Nature Chemistry* 3 (2011): 205–210..

26. G. N. Lewis, M. Calvin, and M. Kasha, "Photomagnetism. Determination of the Paramagnetic Susceptibility of a Dye in Its Phosphorescent State," *Journal of Chemical Physics* 17 (1949): 804–812.

27. W. P. Headden, "Phosphorescence and Luminescence in Calcites," *American Journal of Science* 5 (1923): 314–328.

28. C. M. Sunta, "A Review of Thermoluminescence of Calcium Fluoride, Calcium Sulphate and Calcium Carbonate," *Radiation Protection Dosimetry* 8 (1984): 25–44.

29. G. R. Fonda, "The Preparation of Fluorescent Calcite," *Journal of Physical Chemistry* 44 (1940): 435–439.

30. A. Castro, E. Aguado, J. M. Rojo, P. Herrero, R. Enjalbert, and J. Galy, "The New Oxygen-Deficient Fluorite Bi3NbO7: Synthesis, Electrical Behavior and Structural Approach," *Materials Research Bulletin* 33 (1998): 31–41.

31. M. N. Salimi, R. H. Bridson, L. M. Grover, and G. A. Leeke, "Effect of Processing Conditions on the Formation of Hydroxyapatite Nanoparticles," *Powder Technology* 218 (2012): 109–118.

32. A. Afshar, M. Ghorbani, N. Ehsani, M. R. Saeri, and C. C. Sorrell, "Some Important Factors in the Wet Precipitation Process of Hydroxyapatite," *Materials and Design* 24 (2003): 197–202.

33. L. C. Palmer, C. J. Newcomb, S. R. Kaltz, E. D. Spoerke, and S. I. Stupp, "Biomimetic Systems for Hydroxyapatite Mineralization Inspired by Bone and Enamel," *Chemical Reviews* 108 (2008): 4754–4783..

34. J. Zhang, H. Xu, W. Fang, et al., "Calcium Carbonate as an Ionic Molecular Lock for Ultrastrong Fluorescence of Single Organic Molecules," *Angewandte Chemie International Edition* 64 (2025): e202415664.

35. W. Fang, Z. Mu, Y. He, et al., "Organic–inorganic Covalent–ionic Molecules for Elastic Ceramic Plastic," *Nature* 619 (2023): 293–299.

36. Z. Liu, C. Shao, B. Jin, et al., "Crosslinking Ionic Oligomers as Conformable Precursors to Calcium Carbonate," *Nature* 574 (2019): 394–398.

37. Z. Ma, K. Kong, Y. Yin, et al., "High Mechanical Strength Alloy-Like Minerals Prepared by Inorganic Ionic Co-Cross-Linking," *Advanced Materials* 36 (2024): 2308017.

38. S. Wu, T. Wang, and E. Zysman-Colman, "Hydrogen-Bonded Supramolecular Network Triggers High-Efficiency Blue Room-Temperature Phosphorescence," *CCS Chemistry* 6 (2024): 2727–2740.

39. T. R. Machado, J. C. Sczancoski, H. Beltrán-Mir, et al., "A Novel Approach to Obtain Highly Intense Self-activated Photoluminescence Emissions in Hydroxyapatite Nanoparticles," *Journal of Solid State Chemistry* 249 (2017): 64–69.

40. T. Rivera-Montalvo, R. A. Romero, S. J. Vicencio Hernandez, and V. C. Delgado, "Synthesis and Thermoluminescent Characterization of Synthetic Hydroxyapatite as a Detector for Retrospective TL Dosimetry," *Applied Radiation and Isotopes* 220 (2025): 111790..

41. V. S. Bystrov, J. Coutinho, A. V. Bystrova, et al., "Computational Study of Hydroxyapatite Structures, Properties and Defects," *Journal of Physics D: Applied Physics* 48 (2015): 195302.

42. V. S. Bystrov, L. A. Avakyan, E. V. Paramonova, and J. Coutinho, "Sub-Band Gap Absorption Mechanisms Involving Oxygen Vacancies in Hydroxyapatite," *Journal of Physical Chemistry C* 123 (2019): 4856–4865.

43. V. S. Bystrov, C. Piccirillo, D. M. Tobaldi, et al., "Oxygen Vacancies, the Optical Band Gap (Eg) and Photocatalysis of Hydroxyapatite: Comparing Modelling With Measured Data," *Applied Catalysis B: Environmental* 196 (2016): 100–107.

44. K. Matsunaga, "Theoretical Investigation of the Defect Formation Mechanism Relevant to Nonstoichiometry in Hydroxyapatite," *Physical Review B* 77 (2008): 104106.

45. C. Xiajie, W. Hong, Z. Li, M. Xingtao, Z. Xingdong, and Y. Mingli, "Hydroxyl Migration Disorders the Surface Structure of Hydroxyapatite Nanoparticles," *Applied Surface Science* 416 (2017): 901.

46. W. Xian, Z. Li, Z. Qun, J. Gang, and Y. Mingli, "First-principles Study on the Hydroxyl Migration From Inner to Surface of Hydroxyapatite," *Applied Surface Science* 452 (2018): 381.

47. A. J. Sindt, B. A. DeHaven, D. F. McEachern, et al., "UV-irradiation of Self-Assembled Triphenylamines Affords Persistent and Regenerable Radicals," *Chemical Science* 10 (2019): 2670–2677.

48. C. Adamo and V. Barone, "Toward Reliable Density Functional Methods Without Adjustable Parameters: The PBE0 Model," *Journal of Chemical Physics* 110 (1999): 6158–6170.

49. F. Weigend and R. Ahlrichs, "Balanced Basis Sets of Split Valence, Triple Zeta Valence and Quadruple Zeta Valence Quality for H to Rn: Design and Assessment of Accuracy," *Physical Chemistry Chemical Physics* 7 (2005): 3297..

50. S. Hirata, Y. Sakai, K. Masui, et al., "Highly Efficient Blue Electroluminescence Based on Thermally Activated Delayed Fluorescence," *Nature Materials* 14 (2015): 330–336.

51. H. Uoyama, K. Goushi, K. Shizu, H. Nomura, and C. Adachi, "Highly Efficient Organic Light-emitting Diodes From Delayed Fluorescence," *Nature* 492 (2012): 234–238..

52. H. Tsujimoto, D.-G. Ha, G. Markopoulos, H. S. Chae, M. A. Baldo, and T. M. Swager, "Thermally Activated Delayed Fluorescence and Aggregation Induced Emission With through-Space Charge Transfer," *Journal of the American Chemical Society* 139 (2017): 4894–4900..

53. J. Rao, L. Yang, X. Li, et al., "Meta Junction Promoting Efficient Thermally Activated Delayed Fluorescence in Donor-Acceptor Conjugated Polymers," *Angewandte Chemie International Edition* 59 (2020): 17903–17909.

54. X. Chen, C. Xu, T. Wang, et al., "Versatile Room-Temperature-Phosphorescent Materials Prepared From N-Substituted Naphthalimides: Emission Enhancement and Chemical Conjugation," *Angewandte Chemie International Edition* 55 (2016): 9872–9876.

55. B. Ding, L. Ma, Z. Huang, X. Ma, and H. Tian, "Engendering Persistent Organic Room Temperature Phosphorescence by Trace Ingredient Incorporation," *Science Advances* 7 (2021): eabf9668..

56. C. Yin, S. Sun, Z.-A. Yan, et al., "A Universal Strategy for Multicolor Organic Circularly Polarized Afterglow Materials With High Dissymmetry Factors," *Proceedings National Academy of Science USA* 122 (2025): e2419481122.

57. A. Cheng, H. Su, X. Gu, et al., "Disorder-Enhanced Charge-Transfer-Mediated Room-Temperature Phosphorescence in Polymer Media," *Angewandte Chemie International Edition* 62 (2023): e202312627.

58. T. Wang, J. De, S. Wu, A. K. Gupta, and E. Zysman-Colman, "Thermally Activated and Aggregation-Regulated Excitonic Coupling Enable Emissive High-Lying Triplet Excitons**," *Angewandte Chemie International Edition* 61 (2022): e202206681.

59. T. Wang, A. K. Gupta, D. B. Cordes, A. M. Z. Slawin, and E. Zysman-Colman, "Reducing Efficiency Roll-off in Multi-Resonant Thermally Activated Delayed Fluorescent OLEDs Through Modulation of the Energy of the $T_2$ State," *Advanced Optical Materials* 11 (2023): 2300114.

60. T. Wang, A. K. Gupta, S. Wu, A. M. Z. Slawin, and E. Zysman-Colman, "Conjugation-Modulated Excitonic Coupling Brightens Multiple Triplet Excited States," *Journal of the American Chemical Society* 145 (2023): 1945–1954.

61. T. Wang, Z. Hu, X. Nie, et al., "Thermochromic Aggregation-induced Dual Phosphorescence via Temperature-dependent sp3-linked Donor-acceptor Electronic Coupling," *Nature Communications* 12 (2021): 1364.

## Supporting Information

Additional supporting information can be found online in the Supporting Information section.

**Supporting File 1:** Additional information including chemical sources, methods, supplementary figures and tables has been provided as an individual supplementary material.

**Supporting File 2:** anie72834-sup-0002-MovieS1.mp4.

**Supporting File 3:** anie72834-sup-0003-MovieS2.mp4.